Fast wave heating experiments in the ion cyclotron range of frequencies on ATF

FAST WAVE HEATING EXPERIMENTS IN THE ION CYCLOTRON RANGE OF FREQUENCIES ON ATF

M. KWON*, T.D. SHEPARD, R.H. GOULDING, C.E. THOMAS*,
R.J. COLCHIN, M.R. WADE*, E.F. JAEGER, M.D. CARTER,
F.W. BAITY, D.B. BATCHELOR, G.L. BELL, J.D. BELL**,
T.S. BIGELOW, E.C. CRUME, Jr., A.C. ENGLAND,
J.C. GLOWIENKA, S. HIROE, L.D. HORTON, D.J. HOFFMAN,
R.C. ISLER, R.A. LANGLEY, D.K. LEE**, M. MURAKAMI,
S.L. PAINTER***, D.A. RASMUSSEN, D.W. SWAIN, T. UCKAN,
J.B. WILGEN, W.R. WING
Oak Ridge National Laboratory,
Oak Ridge, Tennessee,
United States of America

ABSTRACT. Fast wave heating experiments in the ion cyclotron range of frequencies (ICRF) were performed on target plasmas produced by 350 kW of electron cyclotron heating at 53 GHz and also by neutral beam injection in the Advanced Toroidal Facility (ATF). Various heating regimes were investigated in the frequency range between 9.2 MHz and 28.8 MHz with magnetic fields of 0.95 T and 1.9 T on axis. The nominal pulse lengths of up to 200 kW RF power were in the range between 100 and 400 ms. Data from spectroscopy, loading measurements, and edge RF and Langmuir probes were used to characterize the RF induced effects on the ATF plasma. In the hydrogen minority reigme at low plasma density, large suprathermal ion tails were observed with a neutral particle analyser. At high density ($\bar{n}_e \geq 5.0 \times 10^{13}$ cm^{-3}) substantial increases in antenna loading were observed, but ICRF power was insufficient to produce definitive heating results. A two-dimensional RF heating code, ORION, and a Fokker-Planck code, RFTRANS, were used to simulate these experiments. A simulation of future high power, higher density experiments in ATF indicates improved bulk heating results due to the improved loading and more efficient thermalization of the minority tail.

1. INTRODUCTION

Heating in the ion cyclotron range of frequencies (ICRF), which is one of the most promising supplemental heating methods for fusion plasmas, was first demonstrated in a non-axisymmetric device, the B-65 racetrack stellarator, in 1958 [1, 2]. Even though fairly extensive ICRF heating experiments were conducted in this device and its successors (B-66 mirror [3] and the Model C stellarator [4-6]), the most successful heating experiments have been performed in tokamaks since the tokamak concept was introduced

in the late 1960s. There were a number of ICRF related experiments, however, in the Uragan series [7] and the L-2 stellarator [8] in the USSR, the Wendelstein series [9] in Germany, the Heliotron series [10-12] in Japan and the Proto Cleo stellarator [13] in the USA. In the late 1980s, the Advanced Toroidal Facility (ATF) was designed and built at Oak Ridge National Laboratory (ORNL) [14] to explore the advantages of the stellarator, for example steady state and currentless operation.

In currentless devices such as the ATF and Heliotron E stellarators, auxiliary heating is necessary to achieve enhanced plasma parameters not provided by the plasma initiation method — electron cyclotron heating (ECH) for the ATF and the Heliotron E devices. ICRF heating (ICRH) was considered as a supplemental heating method in ATF.

Even though ICRH has been used in stellarators since 1958, many aspects of it are not well understood. Only a few ICRH experiments have been

conducted in non-axisymmetric systems, and the development of theory and technology is just beginning. The heating efficiency of ICRF in stellarators is comparable to that in similar sized tokamaks [11], but detailed studies of ICRF induced fast ion confinement and characterization of the effects of ICRF on the plasma parameters in a non-axisymmetric magnetic geometry remain to be done. In this paper, we report our initial analyses of fast ion generation and confinement, and observations of other effects during ICRH experiments on the ATF stellarator.

The fast wave branch must be used in stellarators because the slow wave cannot propagate into the central regions of high density plasmas, as demonstrated by experiments in Heliotron E [11], and because an antenna launching slow waves would have to be located on the high field side, which causes technical difficulties in stellarators for a complicated, state-of-the-art antenna. In Heliotron E, simple, high field side antennas were used. In ATF, the ICRH antenna is located on the low field side and only the fast wave branch is used.

This paper is organized as follows. In Section 2, the ATF device, diagnostics and RF system are described.

In Section 3, the loading data and an interpretation are presented. In Section 4, observations of fast ion generation are shown and analysed. In Section 5, other ICRH effects on plasma parameters are reported. In Section 6, modelling and discussions of the power balance and high density experiments are presented. A summary is given in Section 7.

2. EXPERIMENTAL ARRANGEMENT

ATF is a torsatron-type stellarator with two helical field coils ($\ell = 2$) and 12 field periods (m = 12). Figure 1 is a top view of ATF, showing the locations of the major diagnostics. The fast wave antenna, two RF probes and a Langmuir probe are located at the same port; another RF probe is located at an adjacent port. A scannable neutral particle analyser (NPA) measures the ion distribution. Spectrometers include a grazing incidence spectrometer, a vacuum Czerny–Turner spectrometer and a visible spectrometer. Two pumped limiters, the electron cyclotron emission (ECE) system, the Thomson scattering system, and a 2 mm microwave interferometer are located around the torus. The ECH inputs come from two top ports near
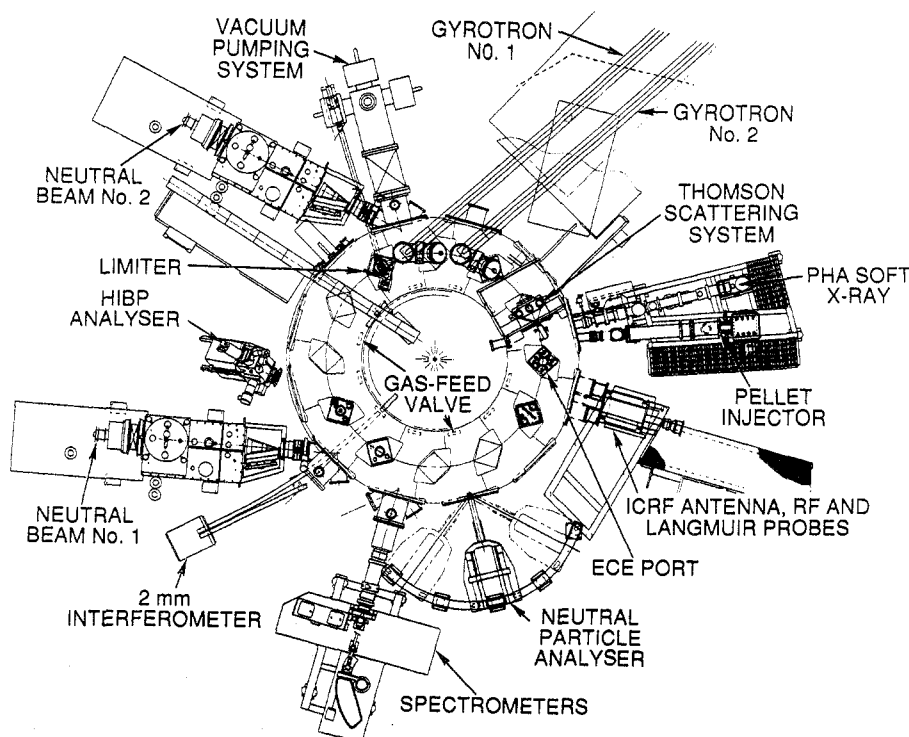

FIG. 1. Top view of the ATF with diagnostics.

the Thomson scattering system, and gas feed valves are located at two inner ports.

Target plasmas for the ICRH experiments were generated by ECH, using either one or two 53 GHz, 200 kW gyrotrons. With the exception of the hydrogen second harmonic experiments, all data were taken in the second phase of operation after the correction of field errors [15], when the profiles of electron temperature and density were broader than those observed during initial ATF operation. Gettering with six titanium sources was normally done in the morning before each run and often had to be repeated midway through the day to maintain control of the density. Table I shows the principal parameters for the target plasmas used for these experiments.

Figure 2 shows a typical ATF magnetic geometry with the antenna located for normal ICRF operation. The mod-B contours have a saddle point which, owing to toroidal effects, is located slightly to the inside of the magnetic axis, so that a pair of cyclotron resonance

TABLE I. ATF PARAMETERS FOR ICRH TARGET PLASMA

ECH power	350–400 kW
Line averaged electron density	$\sim 6 \times 10^{12}$ cm^{-3}
Central electron temperature	800–1000 eV
Central ion temperature	150–200 eV
Stored energy	1.5–2 kJ
Z_{eff}	2

FIG. 3. ATF antenna. (a) Schematic diagram of the RDL-type ATF antenna. (b) Antenna installed in the ATF vacuum vessel at $\phi = 15°$.
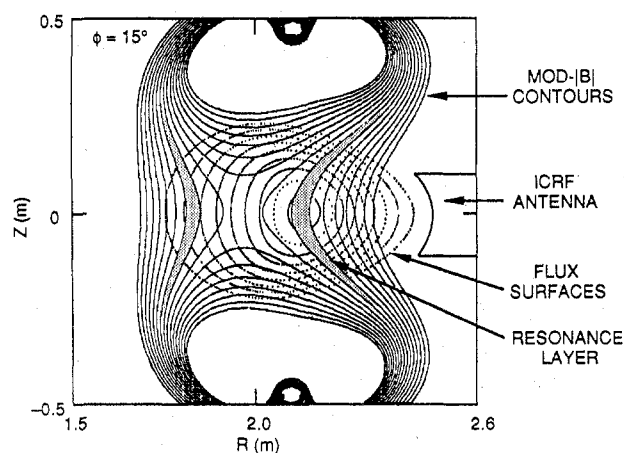

FIG. 2. Typical ATF magnetic geometry at toroidal angle $\phi = 15°$, with the antenna in position for normal ICRH operation. Solid lines: mod-B contours. Dashed lines: flux surfaces. Two resonance layers for 14.4 MHz at 0.95 T are illustrated.
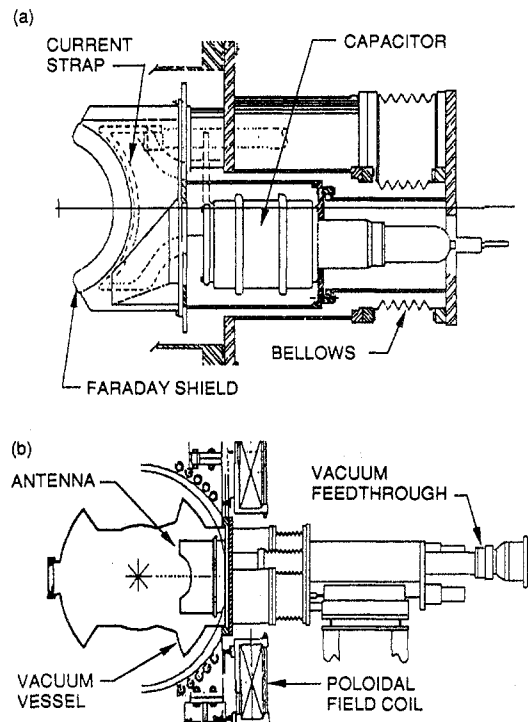
layers is always located either inside and outside or above and below (depending on the toroidal angle ϕ) the saddle point. Usually, for ICRH experiments in this geometry, the RF frequency is determined so that the resonance layer is placed near the magnetic axis. For the minority heating regime, the location of the hybrid resonance layer depends rather sensitively on the minority concentration, owing to the relatively small gradient of mod-B near the saddle point. In ATF, most of the large $k_\parallel$ modes excited by the antenna have thick evanescent regimes for low density target plasmas, typically $\bar{n}_e \leq 0.8 \times 10^{13}$ cm^{-3}. For such plasmas, an antenna with a $k_\parallel$ spectrum in a narrow band around $k_\parallel = 0$ would be preferable. The present ATF antenna design, however, was optimized for higher density and higher power experiments planned for the future.

The ATF ICRF antenna is a resonant double loop (RDL), recessed box antenna, similar to the ICRF antenna constructed at ORNL for the Tokamak Fusion Test Reactor. The ATF antenna was placed on the low field side, unlike the antenna in Heliotron E, which was placed on the high field side. The ATF antenna was also tilted to align it with the local magnetic field line.

The ATF ICRF fast wave antenna, shown in
Fig. 3(a), was designed to launch the fast wave at
power levels of up to 1 MW. It can be moved radially
over a range of 15 cm and has no external cooling
system, since long pulse operation is not foreseen for
this prototype design. This RDL antenna has two
grounded capacitors connected to the ends of the
current strap, with power fed into the strap at a feed
point fixed at an intermediate position. Compared to
other types of antennas, such as a single-loop antenna,
the RDL configuration has advantageous electrical
properties. Since the RDL antenna is matched at the
feed point, it produces relatively low voltages and
currents in the feed line (particularly at the vacuum
feedthrough) so that there is no need for external
tuning elements, resulting in a simplified feed system
and significantly reduced overall cost. The antenna is
tunable over a wide frequency range. For the ATF
antenna, this range extends from 9 to 30 MHz. For
tokamak applications, these advantages must be
weighed against the relative difficulty of fabricating a
structure that can withstand disruption forces, but such
severe forces are not present in stellarators. Figure 3(b)
is a side view of the antenna in place; a cross-
section of the ATF vacuum vessel, the relative antenna
location, the bellows system and the vacuum feed-
through are shown. The current strap was tilted 10°
from vertical alignment to optimize the polarization of
the launched wave by minimizing the $E_\parallel$ components.
Radial translation of the antenna was provided by an
electric motor. A set of bellows was installed between
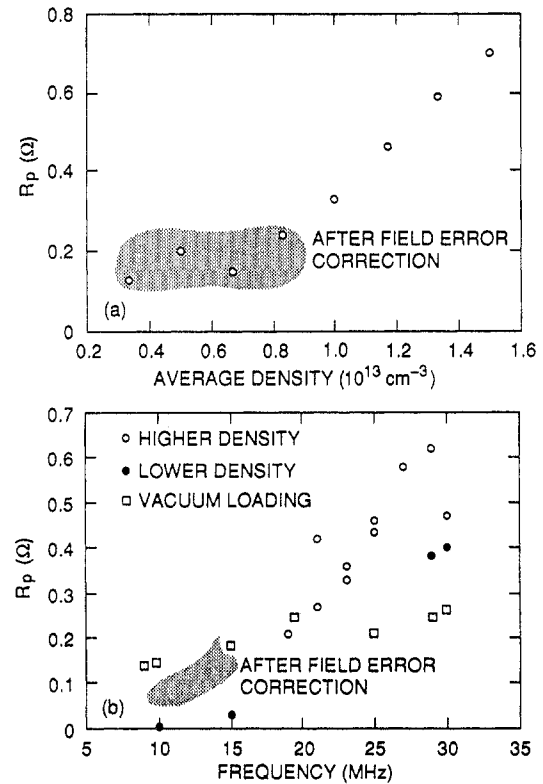the port cover section and the moving carriage section.

FIG. 4. Dependence of the loading on (a) the line integrated
density, with a 28.9 MHz, low power (less than 1 W) RF wave at
0.95 T, and (b) RF frequency. Higher density ($\bar{n}_e \sim 1.6 \times 10^{13}$ cm^{-3})
operations were performed with two neutral beams and lower
density ($\bar{n}_e \sim 1.2 \times 10^{13}$ cm^{-3}) operations with one neutral beam.
The dependence of the measured vacuum loading is also indicated.
The shaded region indicates the loading measured after field error
correction with hydrogen and helium minority ion species.

3. LOADING MEASUREMENTS

Low power loading measurements at 28.8 MHz
were performed during the initial period of ATF
operation in ECH target plasmas with neutral beam
injection (NBI). The 28.8 MHz frequency was equiva-
lent to the second harmonic frequency of hydrogen for
a magnetic field of 0.95 T on the plasma axis. During
this early period of operation, before the correction of
field errors, only one of the two gyrotrons was opera-
tional. Also, gettering during this phase was with
three chromium getter sources instead of the titanium
sources used for the rest of the experiments.
Figures 4(a) and 4(b) show that the loading was very
sensitive to both the plasma density and the frequency
of the RF wave; they include points measured after
field error correction using deuterium plasmas with
hydrogen and helium minorities. However, the loading

was not strongly dependent on the ionic species present,
as determined from measurements made after field
error correction, even though the loading in this phase,
measured mostly at 14.4 MHz and 9.6 MHz, was
slightly higher than that measured before field error
correction. In the D(H) regime (14.4 MHz) the plasma
loading was usually less than the vacuum loading,
which means that more than half of the power was
dissipated in the antenna structure. The D (^{3}He)
regime (9.63 MHz) exhibited the lowest loading.
The measured vacuum loading was proportional to $\sqrt{f}$
within ±10%, as shown in Fig. 4(b).

During operation with only four titanium getter
sources and no extensive antenna conditioning, the
loading for most of the high power ($\sim$ 100 kW)
shots at 28.8 MHz on the low density plasmas
($\bar{n}_e \sim 0.8 \times 10^{13}$ cm^{-3}) peaked in the very early part
of the RF pulse (at 20–30 ms of a 200 ms pulse) and
then decreased to ~ 0.1 Ω for the rest of the RF pulse.

The loading also changed with the RF power level. For 5 and 10 kW of RF power, the loading remained at 0.5 Ω throughout the pulse. Above about 20 kW of RF power, the loading decreased after the initial peak. Clearly, RF power above ~20 kW changed the scrape-off layer (SOL) plasma conditions in front of the antenna within 20–30 ms after RF onset, which changed the antenna loading. This was consistent with the Langmuir probe results for these shots, which showed large changes in n_e and T_e around the antenna for power levels above 20 kW.

After gettering with six titanium sources and extensive antenna conditioning, in the D (H) regime at 0.95 T with 200 kW of RF power at 14.4 MHz the plasma loading increased to 0.2 Ω, slgihtly higher than the vacuum loading. It was also observed that in some shots early in a day of operation the loading did not degrade during the shot. However, as the experiments progressed, the loading dropped to 0.1 Ω, which may have been related to the wall gettering wearing off during the day.

Loading was also strongly dependent on the gap between the plasma and the antenna. The loading decreased exponentially as the antenna was moved out radially for constant plasma conditions [16]. With the antenna pushed in as far as possible and the plasma shifted outward to decrease the gap, the plasma equilibrium changed radically, producing a very low density plasma. Surprisingly, the loading almost tripled. Most of the loading change was probably contributed by edge plasma coupling, since the ICRF wave could not propagate into the low density central plasma region owing to the thick evanescent layer. The RF probes also showed evidence of edge propagation, as discussed in Section 5.
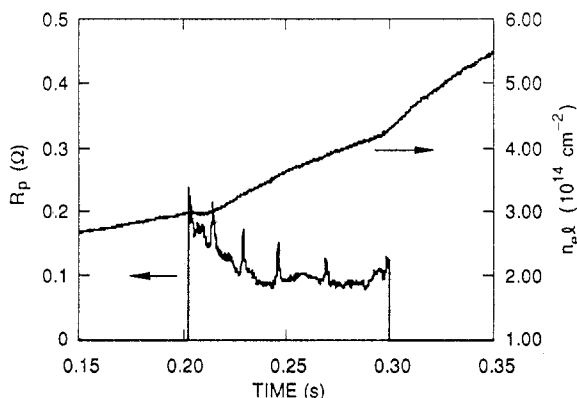
Discrete eigenmodes were observed in the rising density shots, as shown by the peaks in loading in Fig. 5. Ideally, eigenmodes would be identified through systematic measurements at different toroidal and poloidal locations around the vacuum vessel. Since ATF was not equipped with an extensive probe array, a detailed study of eigenmodes was not performed. According to the modelling results discussed in Section 6 and a comparison with other diagnostic signals, however, the observed eigenmode is a toroidal mode which was propagating in the unconfined, edge plasma region.

4. FAST ION STUDIES

Confinement of fast minority ions generated by ICRH is the key factor for success of the minority heating scheme. Significant energetic tails were usually observed with 200 kW of RF power in the minority ion distribution function, as shown in Fig. 6. The tail energies sometimes extended to 50 keV. This tail formation was clearly dependent on the RF power, the RF frequency and the minority concentration. Sometimes the tail would not last until the end of the RF pulse. An example of the temporal behaviour of the energetic tail is shown in Fig. 7(a). During most of the minority ICRH experiments, the NPA data showed an energetic tail up to 30–50 ms after the beginning of RF wave injection, after which the tail energy was significantly degraded. Degradation was also observed in the loading, the stored energy trace and the T_{ECE} trace. The minority species concentration η_H also affected the tail formation. At a fixed power level, a lower minority concentration produced a higher tail energy. Figure 7(b) demonstrates the η_H dependence of the tail formation.

Since energy transfer from the fast ions to the bulk plasma was not observed, understanding these data requires a comparison of the time-scales for the competing energy transfer and loss mechanisms for fast ions. The time-scale for charge exchange loss is given by

$$\tau_{CX} = \frac{1}{n_{neutral} \langle \sigma v \rangle_{CX}} \qquad (1)$$

where $n_{neutral}$ is the neutral density and $\langle \sigma v \rangle_{CX}$ is the charge exchange reaction rate, which is a function of energy. The spatially resolved (or even averaged) neutral density is apparently one of the most difficult quantities to measure in fusion experiments, since it has exponential (or even non-linear) toroidal and poloidal variations

FIG. 5. Discrete eigenmodes in the plasma loading overlapped by the density trace for a 200 kW, 14.4 MHz RF pulse between t = 200 ms and 300 ms.
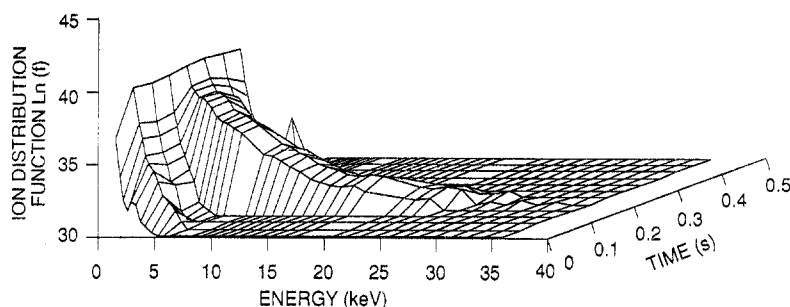
FIG. 6. Three-dimensional view of the evolution of the minority ion (hydrogen) distribution function during minority ion heating in a deuterium plasma with 200 kW, 14.4 MHz RF power at 0.95 T. The RF pulse started at t = 150 ms and lasted for 100 ms.
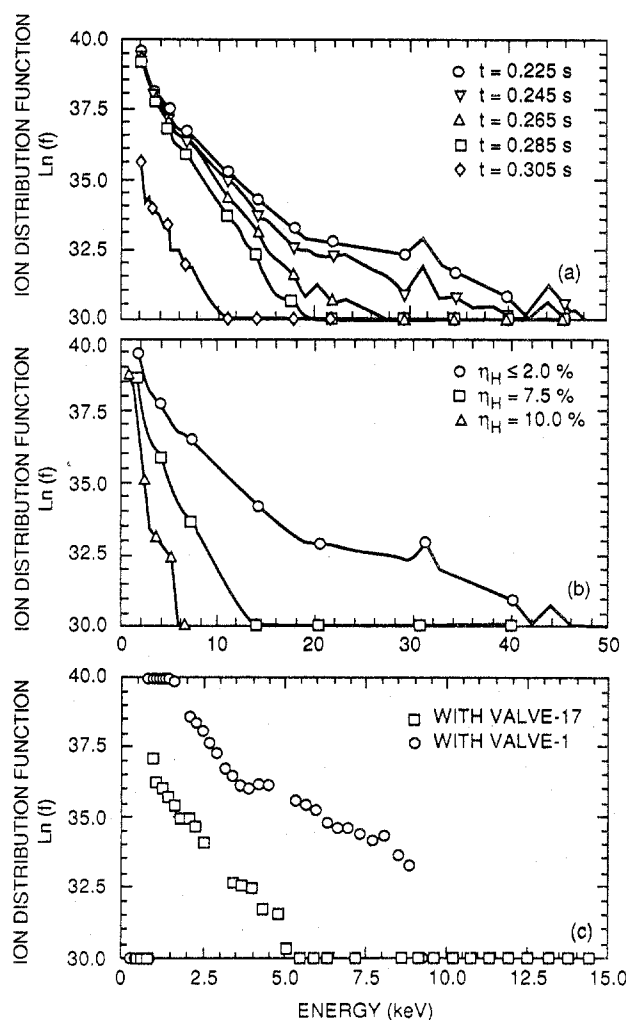

FIG. 7. (a) Temporal evolution of the ion distribution function in a single shot with a 200 kW, 14.4 MHz RF pulse started at t = 200 ms and lasting for 100 ms. The minority ion concentration was less that 5%. (b) Dependence of the energetic minority ion tail formation on the minority ion concentration with a 200 kW, 14.4 MHz RF pulse in deuterium plasmas. All data were measured 50 ms after RF injection. (c) Energetic minority ion distribution functions measured by NPA using two different gas feed valves. Valve 1 is located at the inner port directly opposite the NPA. Valve 17 is located 120° away from valve 1. The data were measured with 100 kW, 14.4 MHz RF wave injection. The minority ion concentration was less than 5%.

(depending on gas sources and recycling points), which means that knowledge of it at any single position does not imply knowledge of it anywhere else [17]. No measurement of the neutral density was attempted in ATF. On the basis of measurements under similar conditions in the Heliotron E plasma [18] we estimate that the central neutral density was of the order of 0.5×10^8 cm^{-3} and the edge neutral density was 0.5×10^9 cm^{-3}. For this case, τ_{CX} is in the range of between 20 and 200 ms for the plasma region where the ions of interest (10–100 keV) are believed to have been created. But this average value at the NPA position depended on which gas feed valve was used. For shots in which the valve facing the NPA was used, τ_{CX} would be much smaller.

The time-scale for hydrogen fast ion energy transfer to electrons can be represented as the energy equilibration time for particle–particle collisions [19]. The time for proton–electron collisions, τ_{pe}, is calculated to be about 50 ms for the typical ATF low density parameters shown in Table I.

The time-scale for hydrogen energy transfer to deuterium, τ_{pd}, is much longer than τ_{pe}. For the parameters of Table I, τ_{pd} is calculated to be about 200 ms.

A comprehensive study of the loss cone in the ATF magnetic geometry was not performed. However, an initial study [20] showed that when the effect of the equilibrium electric field is not included, most of the particles in the edge plasma region are within the loss cone, even for energies of 1 keV. This study also showed that the presence of the radial electric field reduced the loss cone for low energy particles. From the scaling described here, it can be seen that in the plasma edge region of ATF, fast ions generated by RF are rapidly lost owing to unconfined orbits, while in the central region, charge exchange loss competes with electron drag. However, in low density ATF plasmas, as discussed in Section 6, the RF power flux to the central minority ions was very small. Thus, the total

energy transfer to the plasma via electron drag was negligible.

Against this background, the NPA data measured during ICRH can be better understood. Some particles were accelerated to 50 keV energy and confined at least for the charge exchange time-scale. In most of the ICRH experiments, a gas feed valve located at the port facing the NPA was used for gas feed to the experiment; this decreased τ_{CX} given by Eq. (1). However, in experiments with a valve at a different location, the tail energies were different, as shown in Fig. 7(c). The applied RF power in both cases was 100 kW. It should be noted that the slope of the tail energy (temperature) was also changed. When the distant gas feed valve (located toroidally 120° away) was used, the particles heated in the outer region of the torus probably experienced direct orbit loss before they were lost to charge exchange, which would reduce the energetic tail temperature. On the other hand, when the valve facing the analyser was used, in which case τ_{CX} for the edge particles was small, edge heated particles which lay in the lost orbits contributed significantly to the measured energetic tail.

Horizontal and vertical scans of neutral particle energy with the RF power applied were made by moving the NPA between reproducible shots. These scans were performed for three different frequencies, corresponding to different positions of the resonance layer. Data obtained during these scans are shown in Fig. 8. The peak in the distribution occurred with the NPA at an angle away from the perpendicular to the magnetic field direction. This might be an effect similar to the resonance localization phenomenon observed in tokamaks [21-23]. However, the resonance localization and banana trapped particle orbits which appear in tokamak geometry cannot be used to explain these data, primarily because there are few banana trapped particles in the stellarator geometry. When the same analytic calculation as in Ref. [22] was performed for ATF parameters (but for tokamak geometry), it was found that the calculated distribution should be peaked at different angles for the 14.4 MHz and 16 MHz cases, but the measurement showed that the peaks appeared at the same position, as shown in Fig. 8. The effect of absorbed RF power on the particle orbits (especially helically trapped particles) in the stellarator geometry must be considered to resolve this discrepancy.

Figure 8 shows that the minority fast ion tails were present only for a certain range of horizontal angles of the NPA to the magnetic field. For this range of analyser angles, the NPA could detect only particles with small pitch ($v_\perp \gg v_\parallel$). Since toroidal damping of
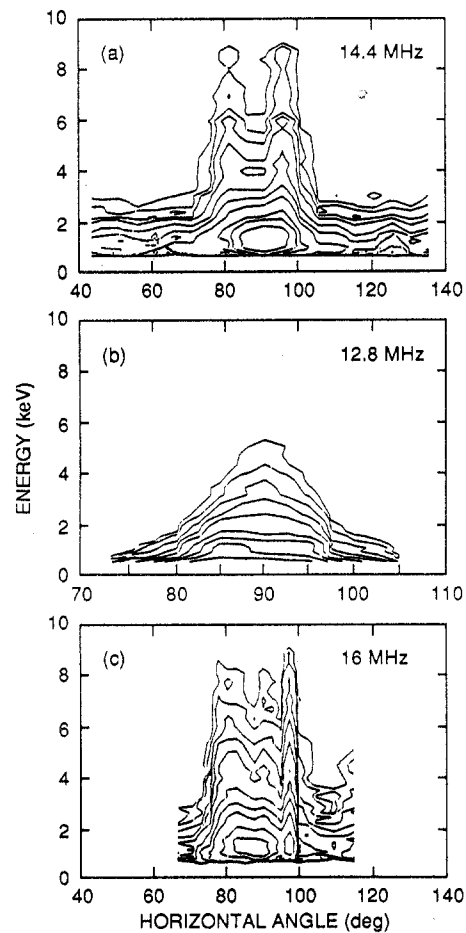

FIG. 8. Energetic minority ion distribution function measured by the NPA, which was moved horizontally between shots, for three different RF frequencies: (a) 14.4 MHz, (b) 12.8 MHz and (c) 16 MHz. All data were measured 20-30 ms after RF wave injection.

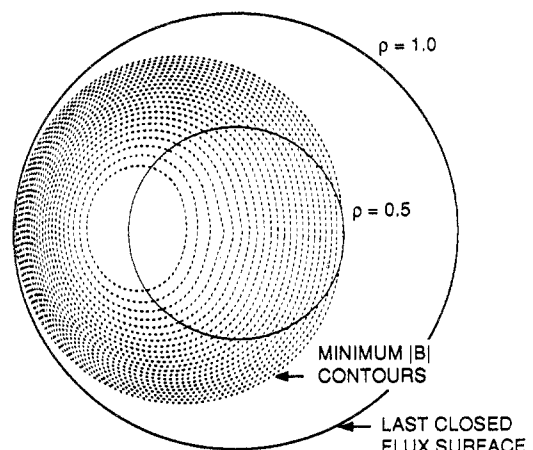FIG. 9. The min-|B| contours in the standard ATF configuration, drawn in Boozer co-ordinates. The ρ = 1.0 circle corresponds to the last closed flux surface, and the ρ = 0.5 circle corresponds to the flux surface with an average radius that is half of the average plasma radius.

the applied RF power was very weak, the effect of locally heated particles near the NPA port could have been dominant, especially for edge heated particles. For the 12.8 MHz case, at the perpendicular analyser angle, in which the resonance layer was isolated near the outside and the inside plasma surface where $n_{neutral}$ was high, locally trapped particles were likely to be charge exchanged immediately, which would increase the NPA measured signal at this angle (90°), as shown in Fig. 8.

There was also an important effect on the particle orbits, related to the configuration of the magnetic field, affecting confinement of the fast ions in ATF. Orbit studies in ATF revealed that the min- |B| contour significantly affects particle confinement [24-26]. In Boozer co-ordinates [27], these contours appear as shown in Fig. 9 for the standard ATF configuration; the closed contour region occurs mainly inside the plasma magnetic axis. The location of the min- |B| contours in ATF can be varied by changing the mid-vertical field coil current. It was found theoretically [24] that as the area of the closed min- |B| contours increases, particle confinement improves. Enhancing the particle confinement by controlling the configuration of the min- |B| contours has been proposed for helical devices [25]. This enhancement occurs because the drift orbits of energetic trapped particles approximately follow the min- |B| contour, according to both analytic (J-invariant) and numerical (guiding centre orbit following code) calculations [26]. If this is the case, particles heated in the inside region (see Fig. 9), where most of the min- |B| contours are closed, would be better confined.

Unlike in tokamaks, where the number of banana trapped particles is large, in stellarators the helically trapped particles may play a major role because the ripple in the magnetic field is larger than that in tokamaks. Particles heated at major radii in the outer region beyond the plasma centre ($R \geq R_0$), where the mirror ratio is large, are likely to be lost because of large ∇ |B| orbit drifts. However, particles heated on the inside can follow a closed min- |B| contour and be confined longer. Deeply helically trapped particles can absorb large amounts of RF energy, since they stay longer in the resonance layer. In the central region of a stellarator, the number of helically trapped particles is so small that the contribution to heating from trapped ions is small. In the edge at large major radii ($R \geq R_0$, as before), a large fraction of the ions are trapped and easily absorb RF energy, but, owing to the large loss cone in this region, these ions are likely to be lost before transferring energy to other particles.

Therefore, in ATF, for good fast ion confinement, RF power deposition should occur in the region where there are closed min- |B| contours and a larger number of trapped particles, i.e. well inside the magnetic axis.

5. EFFECTS ON OTHER PARAMETERS

Typical impurity line signals with ICRH are shown in Fig. 10(a). An RF power threshold was observed at around 40 kW after the start of the first six-element titanium gettering cycle. After extensive six-element titanium gettering on ATF, most of the carbon lines disappeared, while the signal from the C II monitor was still significant. This is attributed to the fact that the impurity monitor has a relatively wide wavelength band, so that other low charge states of high-Z impurity lines made contributions rather than carbon. The Fe XVI emission signals showed slight increases during ICRH, which suggests fast ion loss leading to increased wall sputtering during ICRH.

A vacuum Czerny-Turner spectrometer was used for measuring ion temperatures from Doppler broadened impurity lines. Usually, the O VII line was used for central temperature measurements and the C V line for edge temperature measurements. None of the shots showed any significant increase in central temperature with 200 kW of RF power, while the edge temperature sometimes increased by 5-10 eV. Figures 10(c) and 10(d) show measured ion temperatures with and without RF power for two different radial locations. The Doppler broadened ion temperature measurement shows that the RF power was absorbed away from the centre.

The behaviour of Z_{eff} was determined from bremsstrahlung emission measurements. Usually, ICRH increased the Z_{eff} value by up to 50%. Edge plasmas responded very quickly to the RF wave, no matter where the measurements were made around the torus. The floating potential changed within a few milliseconds after RF wave injection began. The two impurity monitor signals and the line integrated density also responded very quickly.

Figure 10(b) shows the SOL n_e and T_e measurements with a Langmuir probe made during D (H) minority regime ICRH experiments. This direct measurement showed that ICRH increased the SOL temperature and density, which could be interpreted as evidence of direct edge coupling of the RF wave. Because of the high and complex magnetic shear in the edge region of ATF, precise alignment of the RF
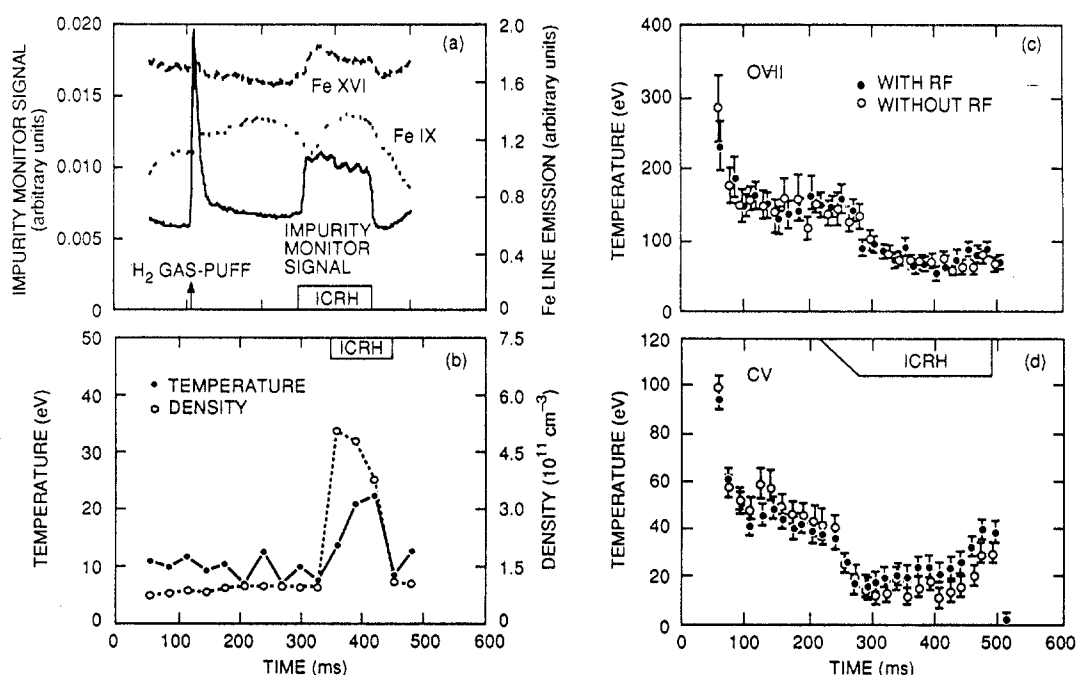
1232

FIG. 10. (a) Typical high-Z impurity line (Fe XVI and Fe IX) emission signals and impurity monitor signal during 200 kW ICRH, measured by a spectroscopic method. (b) Temporal changes in the edge n_e and T_e during D (H) experiments, measured by a Langmuir probe. (c) Ion temperatures with and without ICRH, measured by Doppler broadening of O VIII lines (central plasma regions). (d) Ion temperatures with and without ICRH, measured by Doppler broadening of C V lines (plasma edge region).

probe loops with the local magnetic field was impossible. In this case the data were meaningful when they were compared with a reference signal, such as the probe signals during vacuum-only RF injection. Comparison of a sequence of constant density shots in the D (H) regime, with no eigenmodes, showed little differences in the amplitude at various radial positions. This is evidence of the weak wave propagation inside the plasma.

In most of the shots, higher harmonics of the fundamental RF frequency also appeared on the RF probes, showing some non-linear coupling that may be due to RF sheath effects. No parametric decay instability of the RF was observed during these shots.

6. MODELLING AND DISCUSSION

6.1. Modelling

We modelled the low density ICRH experiments in ATF using ORION, a two-dimensional (2-D) RF heating code [28], and RFTRANS, a Fokker–Planck code [29]. Experimental values were used for most of the required input parameters of the code, including

density and temperature profiles. Table II shows typical input parameters used for simulation of the D (H) experiments.

TABLE II. ATF PLASMA AND VACUUM VESSEL PARAMETERS FOR COMPUTER SIMULATIONS

Central electron temperature, $T_e(0)$	800 eV
Edge electron temperature, $T_e(a)$	20 eV
Central ion temperature, $T_i(0)$	150 eV
Edge ion temperature, $T_i(a)$	15 eV
Central electron density, $n_e(0)$	9×10^{12} cm^{-3}
Edge electron density, $n_e(a)$	2×10^{12} cm^{-3}
Limiter density e-folding length, λ_n	5 cm
Major radius, R	2.1 m
Average minor radius, $\bar{a}$	0.3 m
Minority concentration, $\eta_{minority}$	0.05
Gap between strap and plasma	6 cm
Strap width	10.8 cm
Side wall width	22.0 cm

Re(E⁺)   P_deposited

(a)

(b)

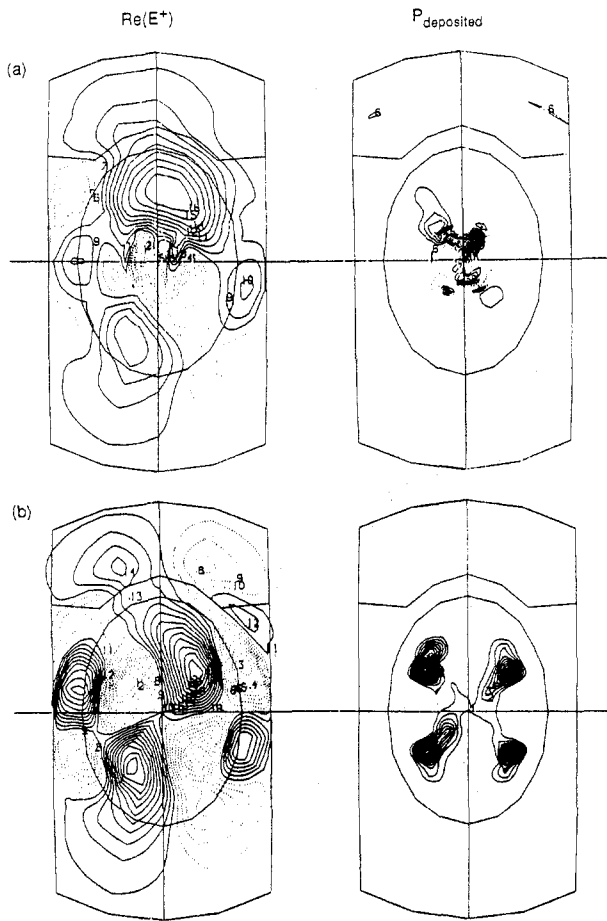FIG. 11. RF field profiles for two $k_\parallel$ modes, (a) $k_1 = 3.8\ m^{-1}$ and (b) $k_\parallel = 10\ m^{-1}$, Profiles of the left-polarized electric fields induced by the ICRF wave and RF power deposition profiles at $\phi = 15°$ for two different wave numbers are shown. Solid lines: positive quantitities; dashed lines: negative quantities. This calculation was done for the parameters in Table II.

tration to the central plasma column, where power can be deposited, was possible. In Fig. 11, contours of constant field and power deposition are shown in the simulated ATF geometry.

The antenna spectrum was primarily determined by the width of the strap and the gap between the side walls. For low density plasmas, the strap (~ 10 cm wide) and the gap between the side walls (22 cm) were too narrow to launch the narrow band of accessible modes (low $k_\parallel$ modes). The side wall image currents affected the spectrum so that low $k_\parallel$ modes were suppressed. The suppressed modes were the ones which would have penetrated to the plasma centre and would possibly have performed useful heating. This situation should improve with the higher density plasmas for which this antenna was designed.

It is interesting to compare the antenna spectrum with and without plasma effects, as shown in Fig. 12. For the vacuum spectrum shown in Fig. 12(a), the peak in B_z appears at $k_\parallel \sim 15$ m⁻¹, but this mode has such a high $k_\parallel$ number that it does not penetrate into

The RF field profiles were different for smaller and larger $k_\parallel$ modes, as shown in Fig. 11. For smaller $k_\parallel$ modes (Fig. 11(a)), the fast wave was able to propagate over most of the region in front of the antenna. For larger $k_\parallel$ modes (Fig. 11(b)), the lower hybrid cut-off layer was located in the plasma region. As a result, the evanescent layer was very thick, making it difficult for this mode to tunnel through it. For the given plasma conditions, the larger mode, $k_\parallel = 10$ m⁻¹, appeared to be the dominant one.

The field profile for this mode showed an eigenmode structure with an odd m-number, but the profile for the $k_\parallel = 3.8$ m⁻¹ mode did not. However, since the $k_\parallel = 10$ m⁻¹ mode had a larger edge evanescent layer, the power deposition was limited to the edge region, while for the $k_\parallel = 3.8$ m⁻¹ mode, good pene-
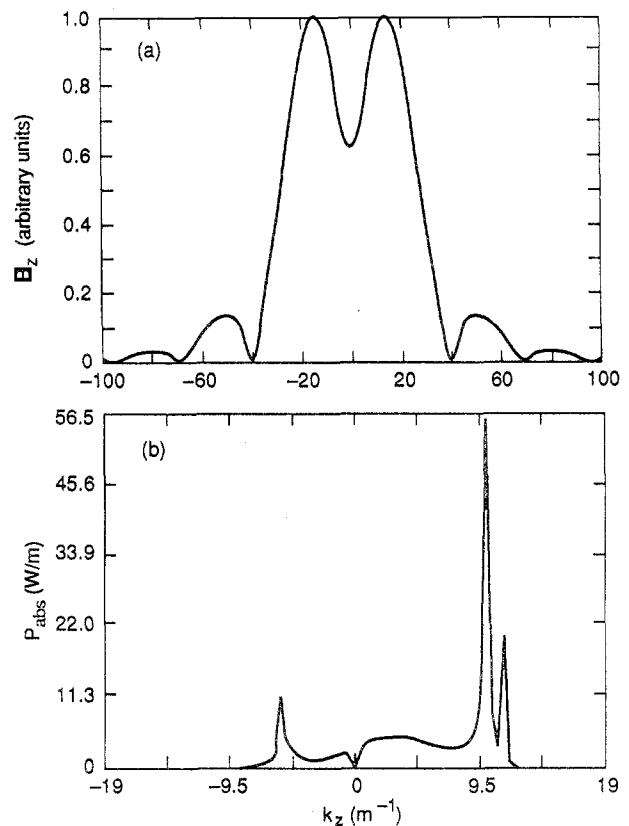

FIG. 12. (a) Antenna spectrum in vacuum, with B_z profile measured 3 cm from the Faraday shield. (b) Antenna spectrum with plasma and absorbed power for a given $k_\parallel$ mode. This calculation was done for the parameters in Table II.
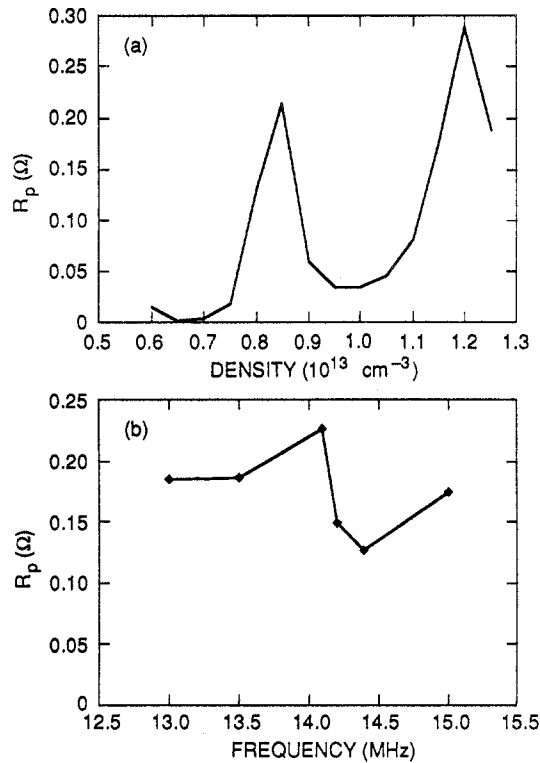
FIG. 13. Calculated dependence of the loading on (a) the density and (b) the frequency. At f = 14.4 MHz, the resonance layer is on the magnetic axis. This calculation was done for the parameters in Table II.

the central plasma column at all. Figure 12(b) shows the absorbed power in the plasma as a function of $k_\|$; in this case, an eigenmode-type power deposition was evident. Note that a dip appears around $k_\| = 0$, and the deposition is asymmetric around $k_\| = 0$. This is caused by the helical configuration and poloidal field effects. When the field is reversed, this asymmetry is also reversed.

Loading is calculated from $\int P_{abs} dV / |I|^2_{ant}$, where P_{abs} is the absorbed RF power and I_{ant} is the antenna current. Although any plasma parameter can affect loading, the loading was experimentally found to be most sensitive to density and frequency. Here the effects of density included the power deposition profile and the gap between the antenna and the plasma. Figure 13(a) shows the calculated dependence of the loading on density. Eigenmodes were observed, but they appeared more often for the same density range in the experiments shown in Fig. 5. Figure 13(b) shows the dependence of the loading on frequency for the D (H) regime in which the frequency of 14.4 MHz placed the fundamental resonance layer on the magnetic axis in the typical ATF ECH plasma. Overall,

the simulated loading data (Fig. 13) matched the experimental data (Figs 4 and 5) quite well in amplitude.

The power deposition profile was calculated with ORION, although, owing to the lack of a kinetic model in the plasma response function, the power partitioning to each plasma species could not be calculated. For higher $k_\|$ modes, as expected, the calculation shows that power was deposited in the off-central region at these low densities. As shown in Fig. 12(b), the $k_\|$ spectrum for power absorption shows that the dominant mode was a single $k_\| = 10$ m^{-1} mode, and the power of this mode was deposited in the outer half-radius. This is reasonable because in the experiments the measured loading was very low, which shows that not much power was absorbed by the plasma, and because edge heating occurred during ICRH. According to the calculation, in a low density plasma little power would go to the central column, significant heating due to the evanescent wave would occur in the plasma edge, and toroidal damping would be very weak. Figure 14 shows the radial profile of the calculated flux surface averaged absorbed power for $k_\| = 10$ m^{-1}. In this case, 80% of the power was deposited in the outer half-radius.

When interpreting the minority charge exchange spectrum, it is not relevant to compare the well known model for T_{eff} of Stix [23] with the measured NPA data because T_{eff} was derived with the Coulomb collision term as a single, dominant energy loss mechanism. For cases in ATF where drift orbit loss of fast ions constituted the major loss channel for the fast ion energy, comparison of the NPA data with Stix's
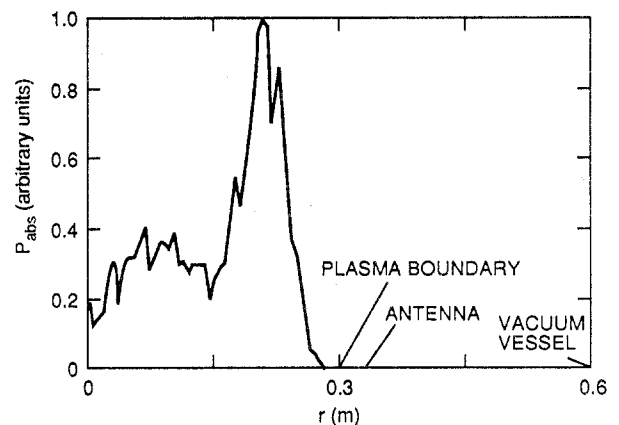

FIG. 14. Radial profile of the calculated flux surface averaged absorbed power for $k_\| = 10$ m^{-1}. This calculation was done for the parameters in Table II.

equation would be unreasonable even if the drift loss term were included, because the basic assumption of Coulomb collisional dominance would still be violated since the drift loss time is shorter than the electron drag time. All of the shots for which the gas feed valve facing the NPA was used fall into this category. The NPA data measured on shots in which this valve was not used showed smaller ion tails, as discussed in Section 4. In this case, since $\tau_{CX} \gg \tau_{loss}$, the contribution of drift loss particles was minimum (they were lost to the walls rather than charge exchanging into the NPA), and the measured NPA ion distributions are believed to represent a quasi-steady-state collision dominated distribution in the plasma.

For this case, the charge exchange loss term and the direct orbit loss term were included in the calculation. Following Stix, the kinetic equation for the ion velocity distribution function including these terms becomes

$$\frac{\partial f}{\partial t} = -\frac{f}{\tau_{CX}} - \frac{f}{\tau_{loss}} + C(f) + Q(f) \qquad (2)$$

where the first term on the right hand side is the charge exchange loss term, the second term is the unconfined orbit loss term, and f is a function of $v_{\parallel}$, $v_{\perp}$, θ and t. Here, τ_{CX} and τ_{loss} are functions of energy. The operators C(f) and Q(f), as given in Ref. [23], are the collision term and the RF contribution to the ion kinetics, respectively. Although τ_{CX} is a function of v, it seems to be reasonable to set it to a constant at any fixed radial position, since the charge exchange cross-section is a very slow function of energy between a few keV and 100 keV.

The RFTRANS code solves a three-dimensional, steady state Fokker–Planck equation. The two velocity space dimensions are the speed v and the pitch angle θ, with a real-space parameter r.

To compare the calculations and the NPA data for the ion distribution, the following assumptions must be made. First, since the calculation was done for a steady state solution, the NPA data must be assumed to represent a quasi-steady state. The NPA data at about 50 ms after the start of the RF pulse were taken as a steady state distribution. Second, τ_{CX} must be much larger than τ_{loss}, otherwise the signal in the NPA is not that of the confined particles but rather that of the lost ones, while f in Eq. (2) is the confined particle distribution function. Only for this case can an ion distribution measured by the NPA be compared with the simulated ion distribution in the loss cone.

The original code has a real-space transport term; however, it was ignored in these calculations, and the kinetic equation used for the steady state condition was

$$-\nu f(v, \theta) + S + C(f(v, \theta)) + Q(f(v, \theta)) = 0 \qquad (3)$$

where ν is the loss rate modelled as discussed below and S is a constant source rate (to compensate for drift orbit losses), which was needed for a steady state solution. Assuming that passing particles are diffusive and well confined and that only trapped particles are convective, we calculate the drift velocity consisting of the curvature and ∇B drifts as

$$v_D \simeq \langle v_{R_c} + v_{\nabla B} \rangle \simeq \frac{v^2}{2R_c\Omega} \qquad (4)$$

where R_c is the radius of the curvature and Ω is the cyclotron frequency. The loss rate in this case becomes

$$\nu \simeq \frac{v_D}{a} \simeq \frac{v^2}{2aR_c\Omega} \qquad (5)$$

where a is the loss radius (which was taken to be the minor radius). This loss rate was compared with the 90° collision rate in order to compensate for any scattering back into the confined regime.

The plasma was divided into two regions. One region represented the central column of the plasma where fast ion confinement was relatively good, while

TABLE III. INPUT PARAMETERS FOR THE FOKKER–PLANCK MODEL OF THE ATF ICRH EXPERIMENT MINORITY FAST ION DISTRIBUTION

$T_e(1)$	830 eV
$T_e(2)$	600 eV
$T_D(1)$	200 eV
$T_D(2)$	150 eV
$T_H(1)$	200 eV
$T_H(2)$	150 eV
$n_e(1)$	6.6×10^{12} cm^{-3}
$n_e(2)$	5.4×10^{12} cm^{-3}
$n_D(1)$	6.3×10^{12} cm^{-3}
$n_D(2)$	5.1×10^{12} cm^{-3}
$n_H(1)$	3.1×10^{11} cm^{-3}
$n_H(2)$	2.6×10^{11} cm^{-3}
$P_{RF}(1)$	0.17×0.027 kW/cm^3
$P_{RF}(2)$	2.0×0.027 kW/cm^3
Major radius R	2.1 m
Average minor radius $\bar{a}$	0.3 m
$R_m(1)$	1.05
$R_m(2)$	1.17

the other region represented the plasma edge where the fast ions produced by RF drifted out quickly, as discussed previously. In this model there was no coupling between these two regions, i.e. no real-space transport. The RF power deposited in each region was estimated from the ORION code.

To evaluate the validity of the model, a qualitative comparison with the NPA data was attempted. Table III shows the parameters used for calculations reflecting typical D (H) heating experiments. Values for the central region are labelled (1) and values for the edge region (2). On the basis of the ORION code results, it was assumed that the RF power was deposited uniformly in the toroidal direction and that most of the power was absorbed in the outer edge region around the resonance layer.

There were two controllable free parameters. One was the RF power density, which was much higher than for a uniform distribution model. Since most of the RF power was deposited along the resonance layer, a weighting factor was used to multiply the value for the uniform distribution case. In Table III, P_{RF} is described as a constant multiplied by 0.027 kW/cm^3, which was the power density with 100 kW of RF power uniformly distributed throughout the ATF plasma volume. The other important free parameter was the loss cone definition. The mirror ratio, defined as $1/R_m = \sin^2\theta$, was used to determine the loss cone angle θ from the $v_\perp = 0$ axis. The values $R_m = 1.05$ and $R_m = 1.17$ were used for the central and the edge loss cone mirror ratios, corresponding to $\theta = 77.4°$ and 67.6°, respectively.

The calculation showed that 40 kW out of 100 kW was absorbed by the plasma, and 80% of the absorbed power was absorbed in the outer region, where the fast ions were only briefly confined. The rest of the power was absorbed in the central region, where the fast ions were better confined. The ion distribution calculated for these data agrees well with the measured NPA ion distribution and gives reasonable values for the confinement times in each region. These calculations indicated that a moderate energy ion tail (up to 10 keV) was formed in the edge region, as shown in Figs 15(a) and 15(b). The slope of the calculated value, the temperature, is comparable to that of the measured ion tail, as shown in Fig. 15(a) for cases in which the gas feed valve facing the NPA was not used. The calculated power transfer to the electrons was about 80% for the central region and 10% for the edge region. It was calculated that 90% of the power in the edge region was lost through the drift orbit loss channel. The calculated fast ion energy confinement times were
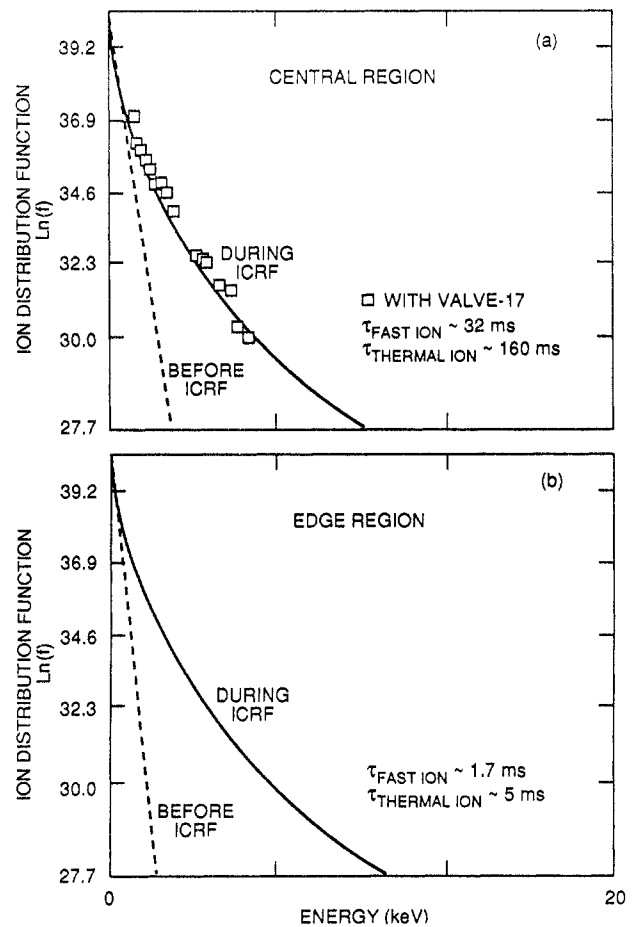

FIG. 15. Calculated energetic minority ion distribution function at (a) the central region (point 1) overlayed with the NPA data shown in Fig. 7(c) (square), and (b) the edge region (point 2). Dashed lines represent the thermal distributions in both regions before RF heating. This calculation was done for the parameters in Table III.

32 ms in the central region and 1.7 ms in the edge region, and the thermal ion confinement times were 160 ms in the central region and 5 ms in the edge region. These fast ion confinement times could not be confirmed experimentally owing to a lack of knowledge of the neutral density profile, the absolute calibration of the NPA and the absolute measurement of the creation rate of fast ions.

6.2. Experiments in high density plasmas

The density limit in ATF ECH plasmas arises from the cut-off density for propagation of the ECH wave. For ECH at 53 GHz, this limit is $\bar{n}_e \sim 0.8 \times 10^{13}$ cm^{-3}. A dense target plasma can be obtained by using NBI created plasmas as a target for the ICRH.

The plasma density of neutral beam heated target plasmas was 8.0×10^{13} cm^{-3} with a ~ 100 ms quasi-steady-state period. The biggest problem was the difficulty in controlling the hydrogen minority concentration because of considerable prior operation in hydrogen. This problem can be resolved by using a helium neutral beam. Another concern was that the available RF power (~ 200 kW) is small compared to the NBI power (≥ 1 MW). Because of the low RF power available for these initial experiments, high density operation was de-emphasized, pending availability of two new 1 MW sources planned for the near future.

The simulation model discussed in Section 6.1, which appears to be valid from comparisons with data from the low density ICRH experiments, was used to predict ICRH performance in higher density plasmas. The ORION 2-D heating code results indicated that higher density plasmas ($\bar{n}_e \sim 5.0 \times 10^{13}$ cm^{-3}) would improve loading by a factor of ten, increase the lower $k_{\parallel}$ portion of the spectrum, enhance wave propagation, increase toroidal damping and increase the fraction of RF power deposited in the central plasma region.

The RFTRANS Fokker-Planck code simulation was also performed for these higher density cases with 100 kW power. This time, more power was assumed to be absorbed in the central column (as predicted by the ORION code), and the power density was higher than for the lower density case owing to the higher loading. The results indicated that most of the power ($\geq 90\%$) would be transferred to the background plasmas and that there should be little high energy tail formation at this power level because slowing down would be very fast. Therefore, most of the fast ion energy would be transferred to the background plasmas.

In initial experiments, 100 kW of ICRH power was launched into a target plasma driven with approximately 1 MW of NBI power, in a minority heating regime (helium neutral beams were injected into a deuterium target plasma with a hydrogen minority). The antenna loading increased by approximately a factor of ten over the ECH driven target plasma case, and the stored energy of the plasma was observed to increase by more than 10% when ICRH was injected into the NBI plasma, as opposed to the case where only the NBI power sustained the plasma. No measurable fast ion tails were observed, as predicted for this RF power level. These results, though modest, are nevertheless encouraging, considering the low RF power level. These initial results are shown in Fig. 16.
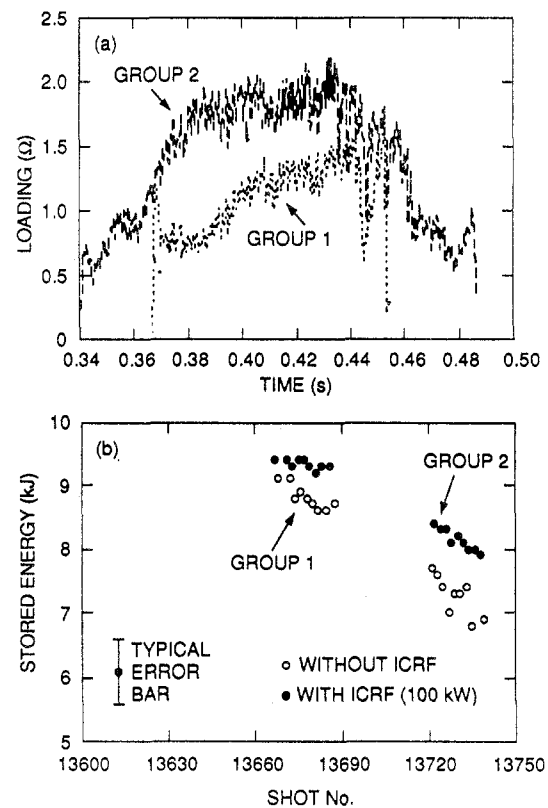

FIG. 16. (a) Measured loading for plasmas heated with helium neutral beams during two different sequences. (b) Changes in stored energy with 100 kW of ICRF on the same plasmas. The average plasma densities were higher than 0.8×10^{14} cm^{-3} and the electron temperatures were less than 0.5 keV. The wave frequencies were 14.4 MHz for group 1 and 14.2 MHz for group 2.

Further high density experiments at higher power are planned for the near future and will be reported in a future paper.

7. SUMMARY AND CONCLUSIONS

We have presented initial results from ICRF heating, primarily of low density ECH produced plasmas, and an analysis of fast ion confinement on ATF. In the second harmonic hydrogen resonant heating regime, it was found that loading was proportional to density and RF frequency, and inversely proportional to the antenna-plasma gap. In full power experiments, loading was measured to be fairly low, as expected by theory, mainly owing to the low density regime explored in these measurements and a large antenna-plasma gap. The low plasma loading led to larger Ohmic loss to the antenna structure — more than half of the transmitter output power.

During low density D (H) heating experiments, NPA signals showed suprathermal minority ion tails up to 50 keV. However, no measurable bulk ion nor electron heating was observed. This was demonstrated to be due to the fact that RF produced fast ions were on unconfined orbits, such that the energy transfer time to the bulk electrons/ions was much longer than the orbit loss time-scale. A principal cause for the heating of particles on loss orbits was the wave spectrum launched by the antenna, which consisted mostly of high $k_\parallel$ modes, such that most of the ICRF power was deposited in the plasma edge region. This was verified by measurements of ion temperatures from Doppler broadened impurity line signals and Langmuir probe measurements. The RF probe also showed that the wave was not propagating well into the confined plasma region, as indicated by comparison with the vacuum signals. During the density ramp, discrete eigenmodes were observed.

A numerical simulation was performed with ORION, a 2-D RF heating code which simulated stellarator magnetic geometry by using helical symmetry. The image currents of the ATF antenna were properly accounted for, yielding good agreement with experimental loading values. Simulations with ATF experimental parameters provided the power absorption spectrum, wave field profiles, RF power deposition, eigenmodes and polarization. A picture consistent with the experimental results was obtained. With a fast ion drift loss term included in the ion kinetic equation, the RFTRANS Fokker–Planck modelling code was used to understand fast ion confinement and RF energy flow to the fast ion channel. A simple ATF plasma model (two-point model) was adopted. Reasonable agreement with the experimental NPA data was achieved.

Predictions for future high density, high power experiments are encouraging and some very preliminary experiments with low power at high density, while not very conclusive, were not at all discouraging.

ACKNOWLEDGEMENTS

REFERENCES

[1] STIX, T.H., PALLADINO, R.W., Phys. Fluids 1 (1958) 446.

[2] STIX, T.H., PALLADINO, R.W., in Peaceful Uses of Atomic Energy (Proc. 2nd Int. Conf. Geneva, 1958), Vol. 31, United Nations, New York (1958) 282.

[3] HOOKE, W.M., ROTHMAN, M.A., SINNIS, J., Phys. Fluids 8 (1965) 1146.

[4] YOSHIKAWA, S., ROTHMAN, M.A., SINCLAIR, R.M., Phys. Rev. Lett. 14 (1965) 214.

[5] CHUNG, K., ROTHMAN, M.A., SINCLAIR, R.M., YOSHIKAWA, S., Phys. Fluids 8 (1965) 1886.

[6] CHUNG, K., ROTHMAN, M.A., Phys. Fluids 10 (1967) 2634.

[7] BAKAEV, V.V., BONDARENKO, S.P., BRONNIKOV, V.V., et al., in Plasma Physics and Controlled Nuclear Fusion Research 1984 (Proc. 10th Int. Conf. London, 1984), Vol. 2, IAEA, Vienna (1985) 397.

[8] BATYUK, V.A., GREBENSHCHIKOV, S.E., KOVAN, I.A., et al., in Heating in Toroidal Plasmas (Proc. 3rd Joint Varenna–Grenoble Int. Symp. Grenoble, 1982), Vol. 1, CEC, Brussels (1982) 273.

[9] CATTANEI, G., ICRF Heating in the WVII-A Stellarator, Rep. IPP2/290, Max-Planck-Institut für Plasmaphysik, Garching (1987).

[10] IIYOSHI, A., SATO, M., SASAKI, A., OBIKI, T., UO, K., Nucl. Fusion 14 (1974) 789.

[11] MUTOH, T., OKADA, H., MOTOJIMA, O., et al., Nucl. Fusion 24 (1984) 1003.

[12] UO, K., IIYOSHI, A., OBIKI, T., et al., in Plasma Physics and Controlled Nuclear Fusion Research 1986 (Proc. 11th Int. Conf. Kyoto, 1986), Vol. 2, IAEA, Vienna (1987) 355.

[13] HOFFMAN, D.J., SHOHET, J.L., Nucl. Fusion 23 (1983) 87.

[14] LYON, J.F., CARRERAS, B.A., CHIPLEY, K.K., et al., Fusion Technol. 10 (1986) 179.

[15] COLCHIN, R.J., HARRIS, J.H., ANDERSON, F.S.B., et al., in Controlled Fusion and Plasma Physics (Proc. 16th Eur. Conf. Venice, 1989), Vol. 13B, Part II, European Physical Society (1989) 615.

[16] GOULDING, R.H., BAITY, F.W., KWON, M., HOFFMAN, D.J., Bull. Am. Phys. Soc. 33 (1988) 1981.

[17] NEILSON, G.H., Charge Exchange Measurements of Ion Behaviour in the ISX Tokamak, PhD Thesis, University of Tennessee, Knoxville (1979).

[18] NAKASHIMA, Y., ZUSHI, H., HANATANI, K., et al., J. Phys. Soc. Jpn. 52 (1983) 4166.

[19] BOOK, D.L., NRL Plasma Formulary, NRL Publ. 0084-4040, Naval Research Laboratory, Washington, DC (1987).

[20] MORRIS, R.N., LYON, J.F., ROME, J.A., Bull. Am. Phys. Soc. 34 (1989) 1948.

[21] KAITA, R., GOLDSTON, R.J., BEIERSDORFER, P., et al., Nucl. Fusion 23 (1983) 1089.

[22] HAMMETT, G.W., Fast Ion Studies of Ion Cyclotron Heating in the PLT Tokamak, PhD Thesis, Princeton, University, Princeton, NJ (1986).

[23] STIX, T.H., Nucl. Fusion 15 (1975) 737.

[24] PAINTER, S.L., LYON, J.F., Fusion Technol. 16 (1989) 157.

[25] CARRERAS, B.A., LYNCH, V.E., DOMINGUEZ, N., LEBOEUF, J.N., LYON, J.F., Confinement Improvement of Low-Aspect-Ratio Torsatrons, Rep. ORNL/TM-11101, Oak Ridge National Laboratory, Oak Ridge, TN (1989).

[26] HEDRICK, C.L., CARY, J.L., TOLLIVER, J.S., Adiabatic and full guiding center motion in 3-D toroidal systems, submitted to Phys. Fluids.

[27] BOOZER, A.M., Phys. Fluids 25 (1982) 520.

[28] JAEGER, E.F., BATCHELOR, D.B., WEITZNER, H., WHEALTON, J.H., Comput. Phys. Commun. 40 (1986) 33.

[29] CARTER, M.D., JAEGER, E.F., BATCHELOR, D.B., Nucl. Fusion 29 (1989) 2141.